THE JOURNAL OF PHYSICAL CHEMISTRY B
A JOURNAL OF THE AMERICAN CHEMICAL SOCIETY

pubs.acs.org/JPCB

Article

Different Binding Modes of SARS-CoV-1 and SARS-CoV-2 Fusion Peptides to Cell Membranes: The Influence of Peptide Helix Length

Hujun Shen,* Zhenhua Wu, and Ling Chen

Cite This: *J. Phys. Chem. B* 2022, 126, 4261−4271

Read Online

ACCESS | Metrics & More | Article Recommendations | Supporting Information

ABSTRACT: Although the amino acid sequences of SARS-CoV-1 and SARS-CoV-2 fusion peptides (FPs) are highly conserved, the cryo-electron microscopy structures of the SARS-CoV-1 and SARS-CoV-2 spike proteins show that the helix length of SARS-CoV-1 FP is longer than that of SARS-CoV-2 FP. In this work, we simulated the membrane-binding models of SARS-CoV-1 and SARS-CoV-2 FPs and compared the binding modes of the FPs with the POPC/POPE/cholesterol bilayer membrane. Our simulation results show that the SARS-CoV-2 FP binds to the bilayer membrane more effectively than the SARS-CoV-1 FP. It is seen that the short N-terminal helix of SARS-CoV-2 FP is more favorable to insert into the target membrane than the long N-terminal helix of SARS-CoV-1 FP. Meanwhile, the potential of mean force calculations showed that the SARS-CoV-2 FP would prefer only one binding mode (N-terminal binding), whereas the SARS-CoV-1 FP has two favorable membrane-binding modes (C-terminal and N-terminal binding modes). Moreover, in the case of SARS-CoV-1 FP binding to the target membrane, the transition between the two binding modes is relatively fast. Finally, we discovered that the membrane-binding mode would influence the helix length of SARS-CoV-1 FP, while the helix length of SARS-CoV-2 FP could be stably maintained in the membrane-bound configurations. This work suggests that the short helix might endow the FP with high membrane-anchoring strength. In particular, the membrane-penetrating residues (Phe, Ile, and Leu) of short α-helix interact with the cell membrane more strongly than those of long α-helix.

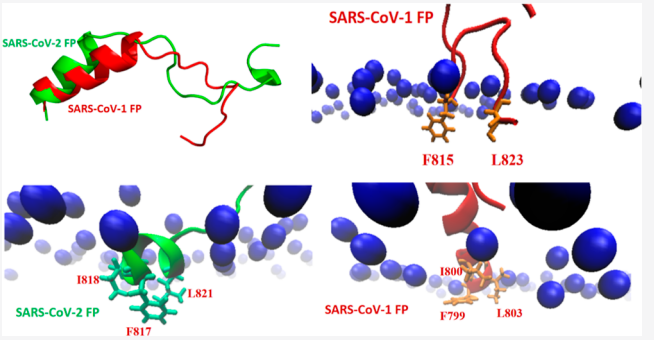

INTRODUCTION

Pneumonia caused by coronaviruses (CoVs) poses a severe threat to public health and seriously hinders economic development. Seven CoVs that can infect human beings have been found. The four CoVs (HCoV-229E, HCoV-NL63, HCov-OC43, and HCoV-HKU1) are relatively mild and generally cause common cold symptoms. The remaining three CoVs (SARS-CoV-1, MERS-CoV, and SARS-CoV-2) have led to the global spread of deadly epidemics. For example, in 2003, the severe acute respiratory syndrome (SARS) caused by SARS-CoV-1 had spread to 29 countries, and more than 8000 cases of SARS-CoV-1 infection were reported worldwide with a mortality rate of nearly 10%.[1] Since the end of 2019, a new CoV (SARS-CoV-2)[2,3] has triggered unprecedented severe pneumonia (COVID-19) worldwide. According to the statistics provided by Johns Hopkins University, by the end of 2021, the cumulative number of confirmed cases in the world have exceeded 280 million and the death toll has exceeded 5.4 million. In particular, the newly discovered SARS-CoV-2 mutants, such as Delta and Omicron variants, have become more infectious, which will continue to bring more significant damage to human health and national economic development.

A SARS-associated CoV (SARS-CoV) is a positive single-stranded RNA virus. The envelope of the virus is mainly composed of lipids and various proteins, including spike protein (S-protein), envelope proteins (E-protein), and membrane proteins (M-protein). In addition, one of the essential proteins in CoV is nucleocapsid protein (N-protein), which is usually employed as a marker in diagnostic assays. Various studies on SARS-CoV-1 and SARS-CoV-2 have shown that the S-protein is essential in viral infection and pathogenesis.[4−9] McLellan et al. determined the cryo-electron microscopy (cryoEM) structure of SARS-CoV-2 S-protein in the prefusion conformation and revealed that the binding of SARS-CoV-2 S-protein with the receptor angiotensin-converting enzyme 2 (ACE2) has a higher affinity than SARS-CoV-1 S-protein.[10] In addition, Zhou et al. determined the complex structure of full-length ACE2 protein and the receptor-binding

Received: February 22, 2022
Revised: May 13, 2022
Published: June 6, 2022

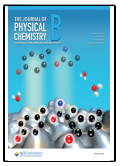

https://doi.org/10.1021/acs.jpcb.2c01295
J. Phys. Chem. B 2022, 126, 4261−4271

domain (RBD) of SARS-CoV-2 S-protein, indicating that the ACE2 protein dimer has "open" and "closed" states. When the S-protein RDB binds to ACE2, the ACE2 dimer will be closed.[11] The S-protein of SARS-associated CoV (SARS-CoV-1 or SARS-CoV-2) contains two subunits (S1 and S2), in which the S1 subunit binds to ACE2 of the host cell through the RBD.[12−16] Then, the S2 subunit promotes the fusion of the virus envelope and the host cell membrane through a series of conformational changes.[17,18]

The S2 subunit of the SARS-CoV S-protein contains multiple potential fusion peptides (FPs), typically composed of 15−40 amino acid residues.[13,19−24] Their interaction with host cells has been widely regarded as the first step of virus host cell fusion.[24,25] For instance, Bosch et al. demonstrated that the region (residues 858−886) in the S2 subunit of SARS-CoV-1 could effectively promote membrane fusion.[20] Sainz et al. defined the two segments (residues 770−788 and 864−886) in the S2 subunit of SARS-CoV-1 as potential FPs.[21] Guillén and co-workers discovered that the segment (residues 873−888) has a high binding affinity with negatively charged phospholipids.[22] Sequence alignment studies revealed that the FP sequence of SARS-CoV-1 (residues 798−815) is highly conserved in the CoV family.[23,26] It is known that this region (residues 798−815) is located at the N-terminus of the S2 subunit following S2′ site cleavage and could induce significant membrane ordering, which is beneficial to the penetration of FPs into the cell membrane.[27] Compared with the type I fusion proteins of HIV and influenza viruses, the existence of multiple potential FPs in the S2 subunit of SARS-CoV S-protein is unique, making the membrane fusion mechanism of SARS-CoVs more complicated.[25]

Given the essential role of FPs in viral membrane fusion, various computational (or theoretical) studies have been carried out to investigate the mechanism of FP−membrane interaction.[28−33] Li and co-workers[30] used the enhanced sampling scheme to address the FP opening of SARS-CoV-2 S-protein, suggesting that the FP opening should occur on the sub-microsecond time scale after S2′ site cleavage. All-atom molecular dynamics (MD) simulation performed by Banerjee et al.[31] showed that the trimeric unit of SARS-CoV-2 FP (residues 816−855) could effectively trigger the initial stages of membrane fusion within hundreds of nanoseconds. Hummer and co-workers[32] used all-atom MD simulations to study the binding of the SARS-CoV-2 FP (residues 816−855) to cellular membranes, finding that two short amphipathic helices ensure high binding strength of the SARS-CoV-2 FP to the cell membrane. Gorgun et al.[33] used the FP segment (residues 798−823) of SARS-CoV-1 S-protein as a template for modeling the membrane binding of SARS-CoV-2 FP (residues 816−841) to the human cellular membrane, revealing three major membrane-binding modes.

Although the FP sequences of SARS-CoV-1 (residues 798−823) and SARS-CoV-2 (residues 816−841) are highly conserved (only two mutated amino acid residues: M816/I834 and E821/D839), the cryoEM studies show a noticeable difference in the structures of SARS-CoV-1 and SARS-CoV-2 FPs.[34−36] In particular, we found that the helix length of SARS-CoV-1 FP (about 1.9 nm) is longer than that of SARS-CoV-2 FP (about 1.1 nm), as shown in Figure 1. Thus, it is necessary to compare the membrane-binding mode of SARS-CoV FPs with different helix lengths or understand how the helix length influences the FP binding to the cell membrane.

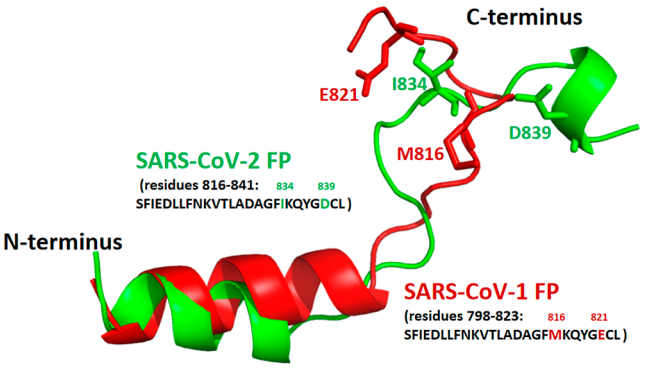

Figure 1. Cartoon representation of the cryoEM structures of the SARS-CoV-1 and SARS-CoV-2 FP fragments (26 amino acid residues), illustrated in red and green colors. The comparison between their sequences shows two mutations: I834/M816 and D839/E821.

In this work, we constructed the membrane-binding models of the SARS-CoV-1 and SARS-CoV-2 FPs with a lipid composition (POPC/POPE/cholesterol: 60/10/30 mol %). For each FP membrane-binding model (SARS-CoV-1 or SARS-CoV-2), we generated six different configurations by changing the angle between the principal axis of the FP peptide and the bilayer normal (z axis) and placing the FP near the bilayer surface with different orientations. We performed a 500 ns MD simulation using the CHARMM36 force field[37] for each configuration. Our all-atom MD simulation results reveal that the membrane binding of SARS-CoV-2 FP is more potent than that of SARS-CoV-1 FP. In addition, we found that the SARS-CoV-2 FP binds to the membrane favorably with its N-terminal while the SARS-CoV-1 FP has no such preference (both the C-terminal and N-terminal binding modes are favorable). Finally, we discovered that the membrane-binding mode would influence the helix length of SARS-CoV-1 FP: the C-terminal loop insertion mode with a short α-helix and the N-terminal binding mode with a long α-helix. In contrast, the short N-terminal helix of SARS-CoV-2 FP can be stably maintained in the membrane-bound configurations, which endows the SARS-CoV-2 FP with high membrane-anchoring strength.

METHODS

Membrane-Binding Models of SARS-CoV-1 and SARS-CoV-2 FPs. To model the SARS-CoV-1 and SARS-CoV-2 FPs (as shown in Figure 1), we used the cryoEM structures of the SAR-CoV-1 S-protein (PDB: 5XLR)[34] and the SAR-CoV-2 S-protein (PDB: 6XR8).[35] The sequence alignment showed two mutations between the FP sequences of SARS-CoV-1 (residues 798−823) and SARS-CoV-2 (residues 816−841): M816/I834 and E821/D839. However, a comparison between the FP structures of SARS-CoV-1 and SARS-CoV-2 displays that the root mean square deviation between them is greater than 5.0 Å. In particular, the helix length of SAR-CoV-1 FP is about 1.9 nm, which is longer than that of SAR-CoV-2 FP (about 1.1 nm).

Based on the web-based CHARMM-GUI platform,[38] we constructed the membrane-binding models of SARS-CoV-1 and SARS-CoV-2 FPs with a lipid composition (POPC/POPE/cholesterol: 60/10/30 mol %). The bilayer membrane contained 180 POPC lipids, 30 POPE lipids, and 90 cholesterol molecules. It is known that phosphatidylcholine

https://doi.org/10.1021/acs.jpcb.2c01295
J. Phys. Chem. B 2022, 126, 4261−4271

(PC) and phosphatidylethanolamine (PE) lipids and cholesterol molecules are predominant components in the cell membrane. In addition, various studies have shown that cholesterol influences the membrane-binding affinity of the SARS-CoV-1 FP[25] and plays a critical role in regulating the organization of the FP in the cell membrane.[39] For each membrane-binding FP model (SARS-CoV-1 FP or SARS-CoV-2 FP), we generated six different conformations by changing the angle between the principal axis of the FP and the bilayer normal (z axis) and placing the FP near the bilayer surface with different orientations, as shown in Figure 2. For each

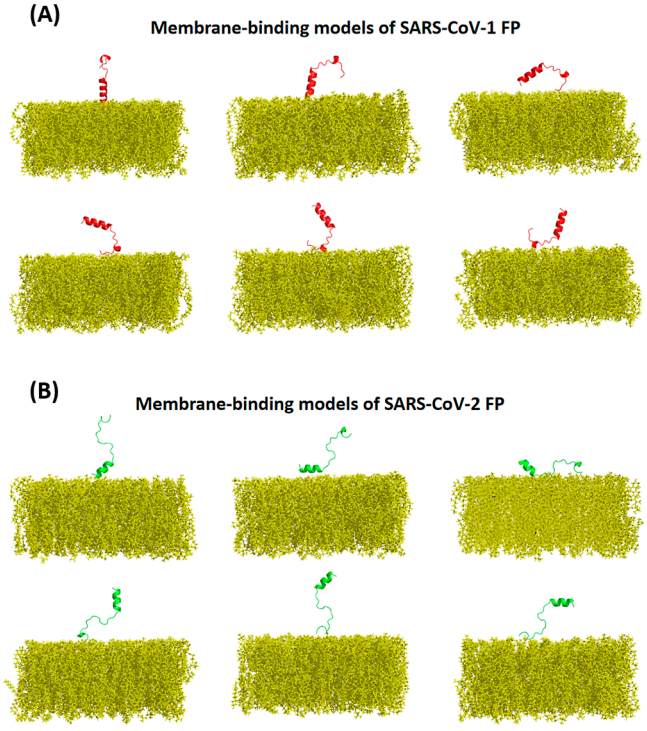

Figure 2. Six membrane-binding configurations of (A) SARS-CoV-1 FP and (B) SARS-CoV-2 FP, used for all-atom MD simulations. The bilayer membrane (in yellow) is composed of POPC, POPE, and cholesterol with a composition (POPC/POPE/cholesterol: 60/10/30 mol %). Cartoon representation of the SARS-CoV-1 and SARS-CoV-2 FP monomers is illustrated in red and green colors, respectively.

configuration, the initial membrane-binding model was respectively immersed in TIP3PS water[40] (a modified TIP3P water model[41] for the CHARMM force field[42]) and ionized with 0.15 M NaCl using the web-based CHARMM-GUI platform.

All-Atom MD Simulations of the Membrane-Bound FP Models. We performed all-atom MD simulations of the membrane-binding models of SARS-CoV-1 and SARS-CoV-2 FPs using the CHARMM36 force field[37] in simulation software GROMACS 4.6.7.[43] For each configuration, we minimized the initial structure (given in Figure 2) using the steepest descent algorithm and then the conjugate gradient algorithm. The minimized system was heated gradually from 200 to 300 K under *NVT* conditions, and a subsequent *NPT* equilibrium run was carried out for 10 ns. Finally, a 500 ns *NPT* production run was performed for final analysis. For each FP model (SARS-CoV-1 FP or SARS-CoV-2 FP), six distinct configurations were simulated respectively for at least 500 ns, and a total of 3.0 μs was used for final analysis. During all *NPT* simulations, a semi-isotropic pressure of 1 bar was maintained using the Parrinello−Rahman algorithm[44] (in the z-direction and x/y plane), and a constant temperature of 310 K was controlled with the Nose−Hoover method.[45,46] All bonds involving hydrogen atoms were constrained using the LINCS algorithm[47] to extend the integration time step to 2 fs. The van der Waals interactions were calculated using the Lennard-Jones potential with a cutoff value of 1.2 nm, and the electrostatic interactions were computed using the Coulomb potential with a cutoff value of 1.2 nm. Meanwhile, we employed the particle mesh Ewald algorithm[48] to treat the long-range electrostatic interactions.

Constant-Velocity Pulling Simulation. We carried out constant-velocity pulling simulations to investigate the binding strength of SARS-CoV-1 and SARS-CoV-2 FPs with the POPC/POPE/cholesterol bilayer membrane. As for each FP model (SARS-CoV-1 FP or SARS-CoV-2 FP), we took six different configurations from 3.0 μs MD simulations and used the six structures as the starting configurations for the constant-velocity pulling simulation. We performed three independent constant-velocity pulling simulations with different initial velocities for each starting configuration. In each constant-velocity pulling simulation, we applied an external force (a force constant of 1000 kJ·nm^{-1}·mol^{-1}) along the z-axis direction between the bilayer membrane center and the FP mass center. We moved the FP mass center away from the bilayer membrane center at a constant velocity of 0.03 nm/ns and stopped the pulling simulation when the FP mass center was 6.0 nm away from the membrane center. All constant-velocity pulling simulations were carried out in the simulation package GROMACS 4.6.7.[43] During all constant-velocity pulling simulations, a semi-isotropic pressure of 1 bar was maintained using the Parrinello−Rahman algorithm[44] (in the z-direction and x/y plane) and a constant temperature of 310 K was controlled with the Nose−Hoover method.[45,46]

RESULTS AND DISCUSSION

Membrane-Binding Strength of SARS-CoV and SARS-CoV-2 FPs. From the all-atom MD simulations of the membrane-binding models of the SARS-CoV-1 and SARS-CoV-2 FPs, we constructed the number density profiles for the phosphate (P) and choline (N) groups of phospholipids, illustrated in Figure S1 of Supporting Information. Based on the number density profiles of the phosphate groups, it is straightforward to calculate the thickness of the POPC/POPE bilayer membrane, which is defined as the phosphate-to-phosphate distance (z-distance). We found that the calculated bilayer thickness with different FPs is about 4.5 nm, indicating that binding different SARS-CoV FPs to the bilayer membrane has a little effect on the bilayer thickness (Figure 3A). Thus, the bilayer membrane surface is defined as the average z-position of the phosphate groups of lipids, which is 2.25 nm from the bilayer membrane center along the z-direction.

Furthermore, from the all-atom MD simulations of the membrane-binding models of the SARS-CoV-1 and SARS-CoV-2 FPs, we calculated the z-distances from the center of mass of the FPs to the bilayer membrane surface, which is defined at the average z-position of the phosphate groups of lipids (or 2.25 nm from the bilayer membrane center). Based on the calculated distance values, we have computed the probability distribution of the distances and then constructed the potential of mean force (PMF) profiles for the binding of the FPs to the POPC/POPE/cholesterol bilayer membrane, as

https://doi.org/10.1021/acs.jpcb.2c01295
J. Phys. Chem. B 2022, 126, 4261−4271

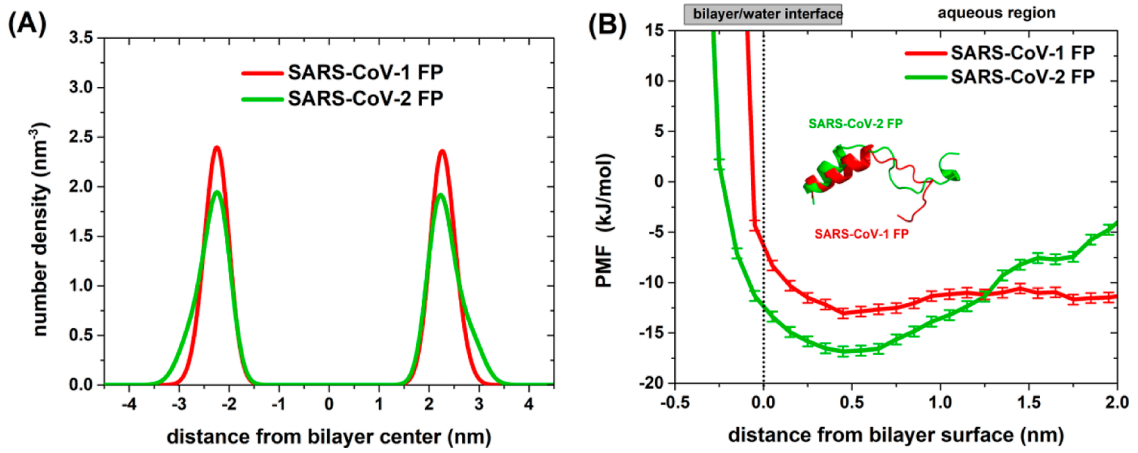

Figure 3. (A) Number density profile for the phosphate (P) groups of phospholipids, obtained from the CHARMM36 all-atom MD simulations of the POPC/POPE bilayer (30% cholesterol) with SARS-CoV-1 (red) and SARS-CoV-2 (green) FPs. (B) PMF profile for binding the SARS-CoV-1 (red) and SARS-CoV-2 (green) FPs to the POPC/POPE bilayer surface. Dotted lines denote the bilayer surface. A negative distance value indicates the location inside the membrane, and a positive value indicates the position outside the membrane. Please note that we used the bootstrapping method to estimate the standard error for the PMF profile.

shown in Figure S2 of Supporting Information. It is shown that different starting orientations of FPs would yield different PMF landscapes. Therefore, we conducted a convergence test by combining the six independent simulations for each FP model, as shown in Figure S3 of Supporting Information. The convergence test showed that the PMF landscapes converge after 1.8 μs simulation (at least 300 ns for each simulation run). From the converged PMF profile (Figure 3B), one can see that the binding of the SARS-CoV-2 FP to the bilayer membrane should be more effective than that of the SARS-CoV-1 FP.

To compare the mechanical strength of FP−membrane binding, we performed constant-velocity pulling simulations on different SARS-CoV-1 and SARS-CoV-2 FP-binding models (Figure S4 of Supporting Information). We carried out three independent pulling simulations with different initial velocities for each starting configuration. In a constant-velocity pulling simulation, we moved the mass center of the FP away from the membrane center along the membrane normal (z axis) until the FP was pulled away from the membrane surface (Figure S5 of Supporting Information). From the force-extension curves (Figure 4), one can see that the maximum rupture forces of SARS-CoV-2 FP-membrane binding models are between 430 pN and 600 pN and those of SARS-CoV-1 FP-membrane binding models are in the range of 250−390 pN, revealing that the membrane-binding strength of SARS-CoV-2 FP is more potent than that of SARS-CoV-1 FP. Thus, the pulling simulation results support the PMF profiles presented in Figure 3B.

According to the number density profiles for water and cholesterol molecules (as shown in Figure 5A,B), we found that the membrane-binding of the SARS-CoV-2 FP (with a short N-terminal helix) caused the displacement of water and cholesterol molecules toward the bilayer membrane center as compared to that of the SARS-CoV-1 FP (with a long N-terminal helix). It is reasonable because the deeper penetration of the SARS-CoV-2 FP into the membrane would affect the distribution of water molecules at the membrane−water interface and that of cholesterol molecules inside the membrane. On the other hand, the displacement of cholesterol molecules toward the bilayer membrane center might benefit the interactions between the SARS-CoV-2 FP and lipids. For instance, from Figure S1 of Supporting Information, one can see that the membrane binding of the SARS-CoV-2 FP makes the density distribution of phosphate and choline groups broader than that of the SARS-CoV-1 FP. In addition, we calculated the interaction site residence times for the specific contacts between the FPs and cholesterol with the PyLIPiD program developed by the Sansom group.[49] By comparing the strength (measured as residue time) of the cholesterol interactions with SARS-CoV-1 and SARS-CoV-2 FPs (given in Figure 5C,D), one can find much stronger cholesterol interactions with the N-terminal residues of SARS-CoV-2 FP than those of SARS-CoV-1 FP. However, we also saw weaker cholesterol interactions with the C-terminal residues of SARS-CoV-2 FP than those of SARS-CoV-1 FP, indicating that the SARS-CoV-2 FP prefers the N-terminal binding to the membrane compared to the SARS-CoV-1 FP.

Binding Modes of the SARS-CoV-1 and SARS-CoV-2 FPs to the Bilayer Membrane. To compare the binding modes of the SARS-CoV-1 and SARS-CoV-2 FPs to the target membrane, we calculated the z-distances from the N-terminus or C-terminus of the FPs to the POPC/POPE/cholesterol membrane surface, respectively. Based on the calculated z-distance results, we constructed the PMF profiles for the N-terminal or C-terminal binding of the FPs to the bilayer membrane, as shown in Figure 6. From Figure 6A, one can see that the N-terminus of the SARS-CoV-2 FP is more deeply inserted in the target membrane than that of the SARS-CoV-1 FP, explaining that the binding strength of the SARS-CoV-2 FP is greater than that of the SARS-CoV-1 FP, as shown in Figure 4. In contrast, the C-terminal binding strength of the SARS-CoV-2 FP is weaker than that of the SARS-CoV-1 FP, presented in Figure 6B. Thus, these results confirm that the SARS-CoV-2 FP binds to the bilayer membrane more favorably with its N-terminus, demonstrated in Figure 5D. Furthermore, Figure 6 shows that both C-terminal and N-terminal bindings of the SARS-CoV-1 FP are favorable, explaining the result given in Figure 5C.

Based on the calculated z-distances from the N-terminus and C-terminus of the FPs to the bilayer membrane surface, we constructed two-dimensional (2D) free energy maps of the FP

https://doi.org/10.1021/acs.jpcb.2c01295
J. Phys. Chem. B 2022, 126, 4261−4271

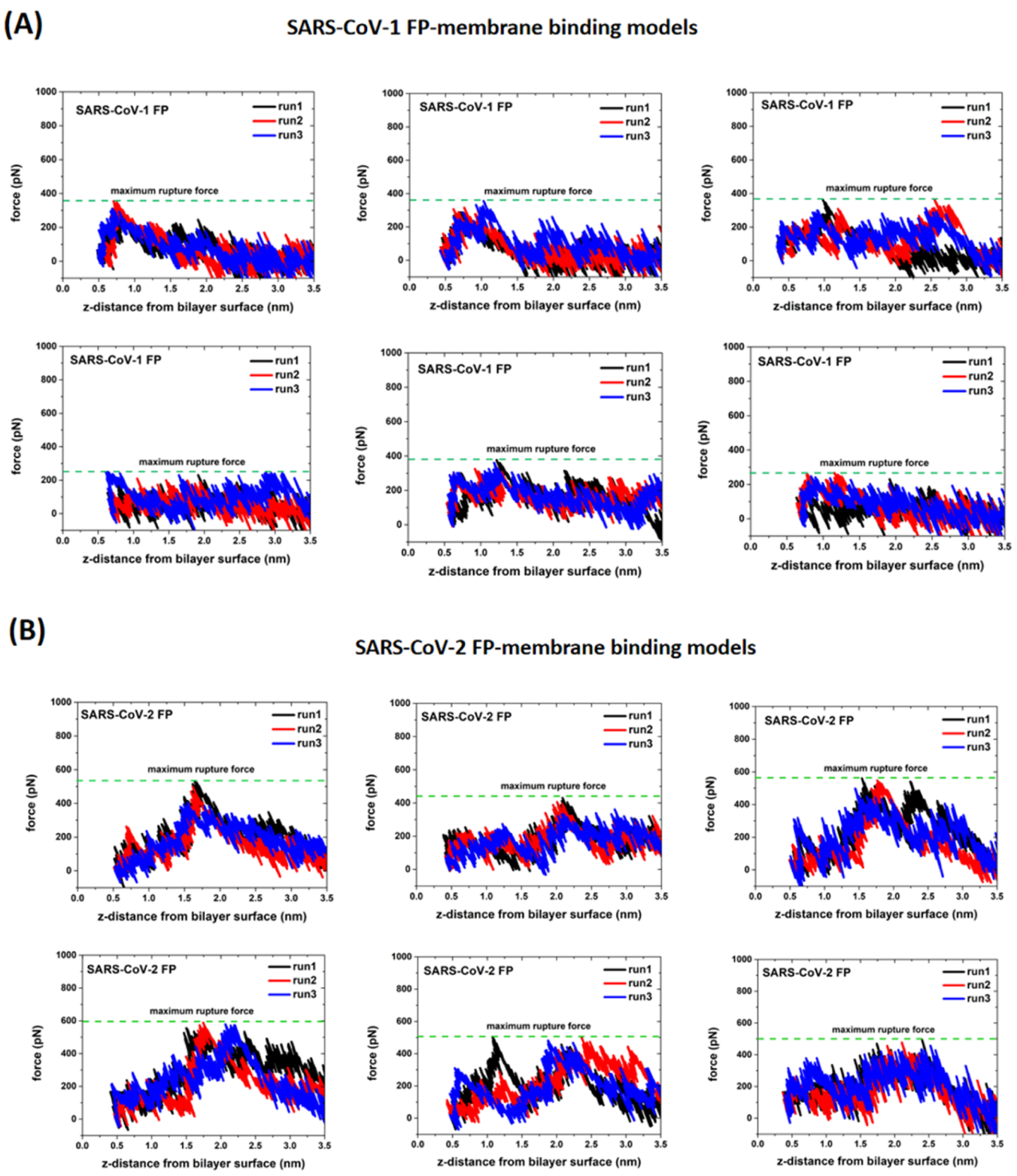

Figure 4. Force−extension curves for pulling (A) SARS-CoV-1 FP and (B) SARS-CoV-2 FP away from the POPC/POPE/cholesterol bilayer membrane surface. For each FP model, six different membrane-binding configurations (given in Figure S4 of Supporting Information) were used for the constant-velocity pulling simulations. Three independent pulling simulations were carried out for each starting configuration with different initial velocities.

binding. In the case of the membrane-bound SARS-CoV-1 FP (Figure 7A), one can see that the SARS-CoV-1 FP has two major binding modes: C-terminal binding and N-terminal binding. Meanwhile, we determined the minimum free energy path (depicted in Figure 7A) based on the calculated PMF values of the conformations, finding that the transition between the two binding modes should be rapid (the free energy barrier between the two binding modes is less than 2 kJ/mol), as shown in Figure 7B. Meanwhile, Figure 7B shows an intermediate state (state III) between the two most favored

https://doi.org/10.1021/acs.jpcb.2c01295
J. Phys. Chem. B 2022, 126, 4261−4271

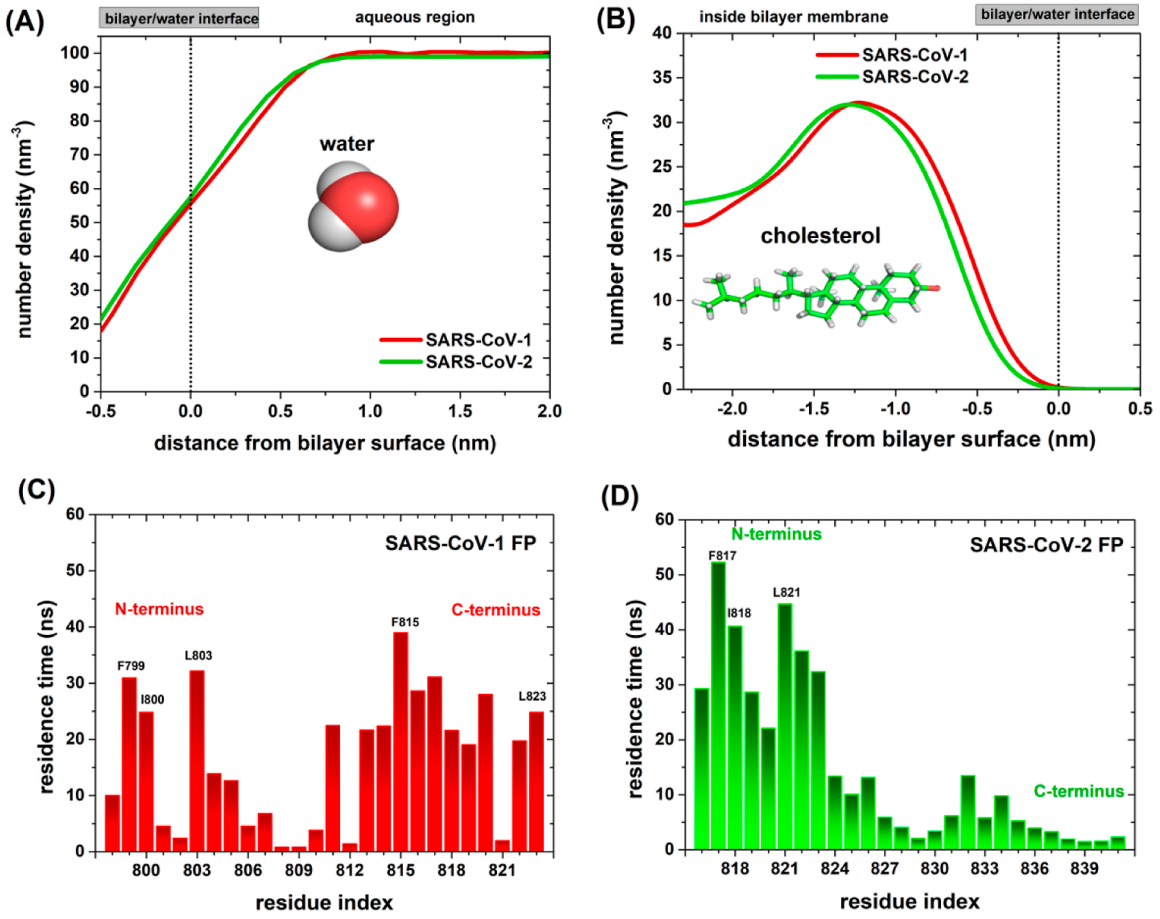

Figure 5. Number density profiles for (A) water molecules and (B) cholesterol molecules, calculated from the all-atom MD simulations of membrane-binding models of SARS-CoV-1 (black) and SARS-CoV-2 (red) FPs. Dotted lines denote the bilayer membrane surface. Interaction site residence time for the specific contacts (C) between SARS-CoV-1 FP and cholesterol and (D) between SARS-CoV-2 FP and cholesterol as a function of the residue index; some penetrating amino acid residues (Phe, Ile, and Leu) are labeled in each figure.

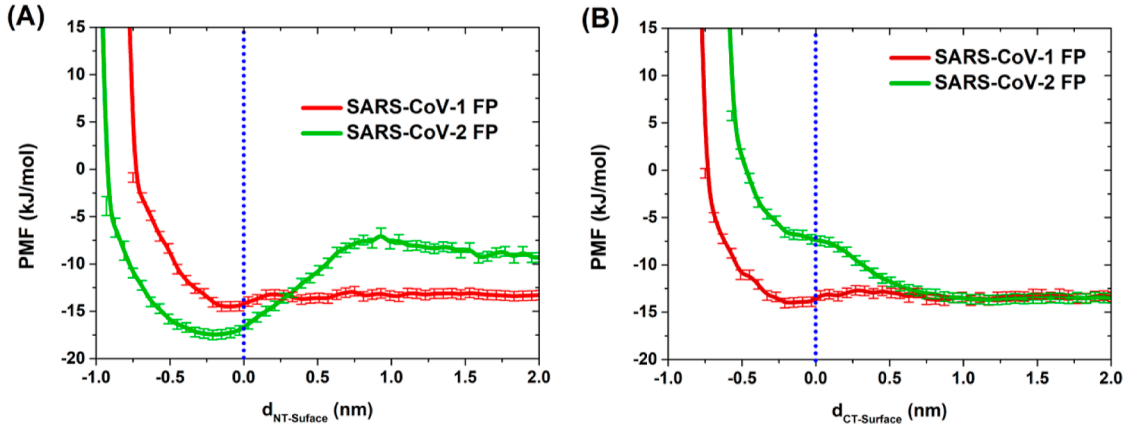

Figure 6. PMF profiles for (A) N-terminal binding and (B) C-terminal binding of the FPs to the POPC/POPE/cholesterol bilayer membrane surface (30 mol % cholesterol), constructed from the all-atom MD simulations of SARS-CoV-1 (red) and SARS-CoV-2 FPs (green) with the bilayer membrane. $d_{NT\text{-}Surface}$ represents the distance from the N-terminus of FPs to the bilayer membrane surface, while $d_{CT\text{-}Surface}$ represents the distance from the C-terminus of FPs to the bilayer membrane surface (denoted by dotted lines). Please note that we used the bootstrapping method to estimate the standard error for the PMF profile.

states (the C-terminal binding and N-terminal binding states, denoted by I and V), and the three membrane-bound states (I, III, and V) are depicted in Figure 7C. The N-terminal binding mode (state V) corresponds to the incomplete insertion of the long N-terminal helix into the bilayer membrane in an oblique manner. In particular, the non-polar side chains of three N-terminal residues (F799, I800, and L803) are buried inside the membrane (Figure S6A of Supporting Information), indicating that the penetrating residues (F799, I800, and L803) are more likely to interact with the membrane, consistent with the result given in Figure 5D. This pattern was also captured by Gorgun et al.,[33] who employed the SARS-CoV-1 FP segment as a

https://doi.org/10.1021/acs.jpcb.2c01295
J. Phys. Chem. B 2022, 126, 4261−4271

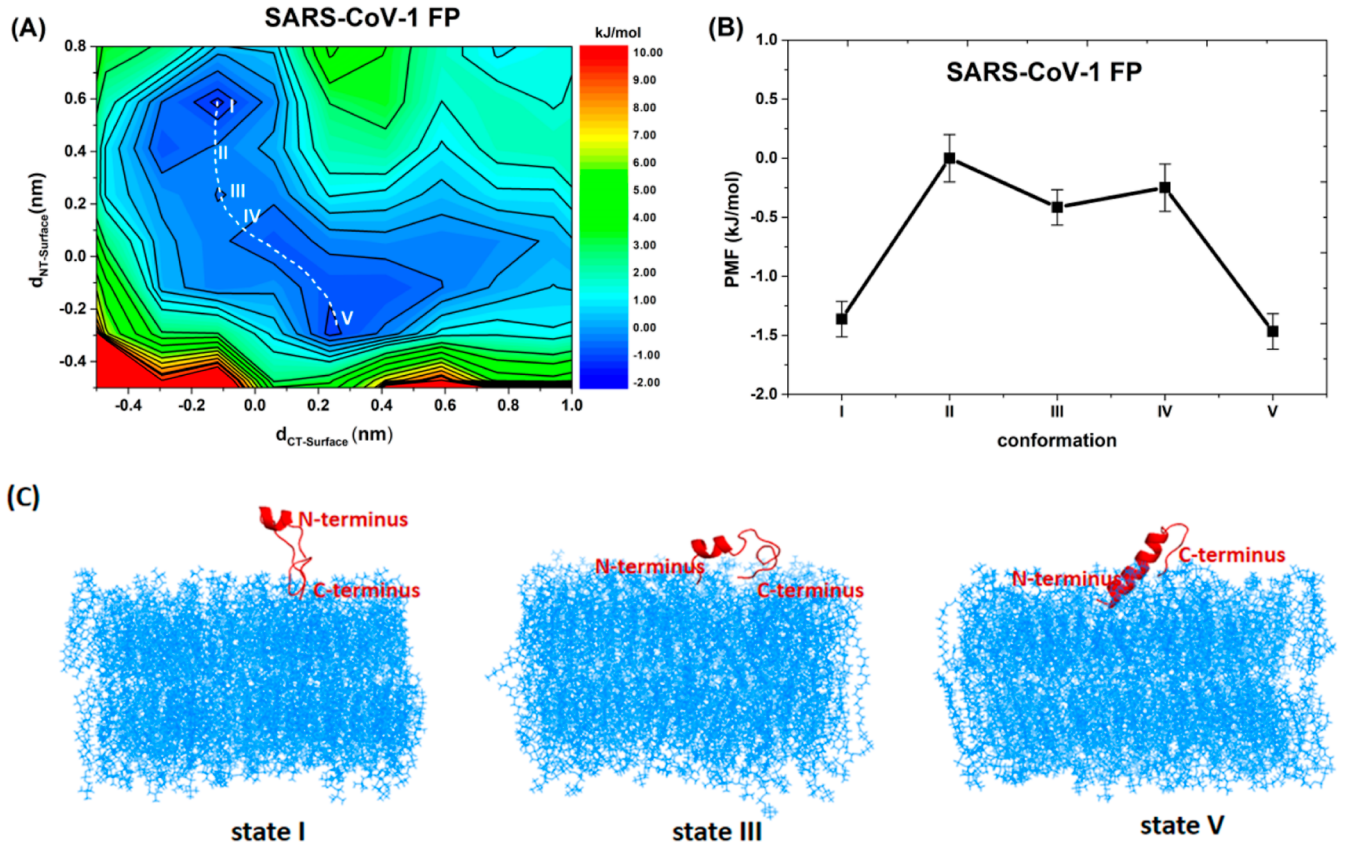

Figure 7. (A) 2D free energy map (kJ/mol) for binding the SARS-CoV-1 FP to the POPC/POPE/cholesterol bilayer membrane. The x axis represents the distance ($d_{CT\text{-}Surface}$) from the C-terminus of the FP to the bilayer membrane surface, while the y axis represents the distance ($d_{NT\text{-}Surface}$) from the N-terminus of the FP to the bilayer membrane surface. The conformations along the pathway from the C-terminal binding mode to the N-terminal binding mode are labeled with I, II, III, IV, and V. (B) Relative free energies (kJ/mol) of five representative conformations along the pathway between two binding modes; please note that the PMF value of state II is taken as the zero free energy. (C) There are three representative snapshots for the membrane-bound states (I, III, and V) of the SARS-CoV-1 FP with the bilayer membrane; the lipid and cholesterol molecules are shown in marine lines and the SARS-CoV-1 FP molecule in a red cartoon.

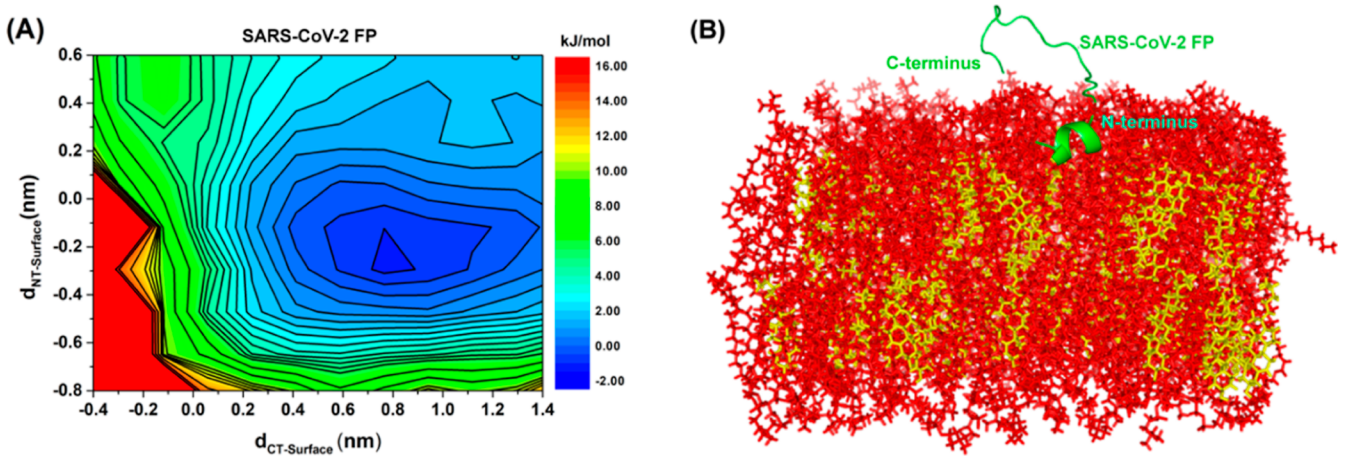

Figure 8. (A) 2D free energy map (kJ/mol) for binding the SARS-CoV-2 FP to the POPC/POPE/cholesterol bilayer membrane. The x axis represents the distance ($d_{CT\text{-}Surface}$) from the C-terminus of the FP to the bilayer membrane surface, while the y-axis represents the distance ($d_{NT\text{-}Surface}$) from the N-terminus of the FP to the bilayer membrane surface. (B) Representative snapshot of the most stable membrane-bound configuration of the SARS-CoV-2 FP with the bilayer membrane, and the lipid and cholesterol molecules are shown in red and yellow sticks, respectively, and the SARS-CoV-2 FP molecule in a green cartoon.

template and simulated the membrane binding of SARS-CoV-2 FP with a highly mobile membrane mimetic model. The transition state (state III) between the N-terminal and C-terminal binding modes shows that the N-terminal helix of the SARS-CoV-1 FP is partially unfolded, and the FP is anchored to the membrane surface through the N-terminus and C-terminus. The C-terminal binding mode (state I) represents a pattern in which the C-terminal loop is inserted in the bilayer

https://doi.org/10.1021/acs.jpcb.2c01295
J. Phys. Chem. B 2022, 126, 4261−4271

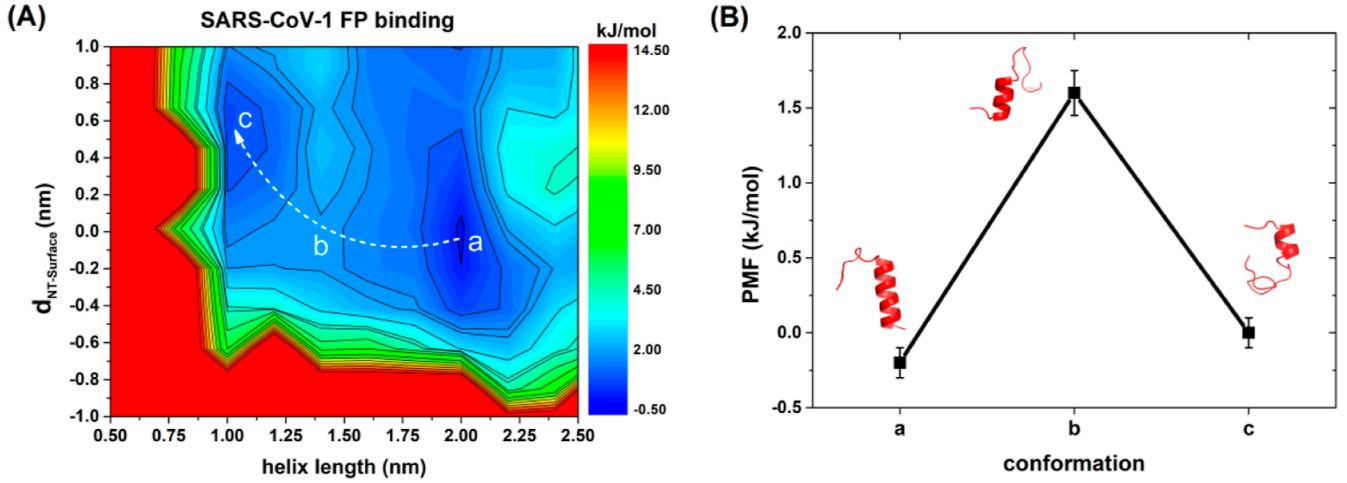

Figure 9. (A) 2D free energy map (kJ/mol) for binding the SARS-CoV-1 FP to the POPC/POPE/cholesterol bilayer membrane. The *x* axis represents the helix length of the FP, while the *y* axis represents the distance ($d_{NT-Surface}$) from the N-terminus of the FP to the bilayer membrane surface. (B) Relative free energies (kJ/mol) of three representative conformations (a, b, and c) with different helix lengths; please note that the PMF value of conformation *c* is taken as the zero free energy.

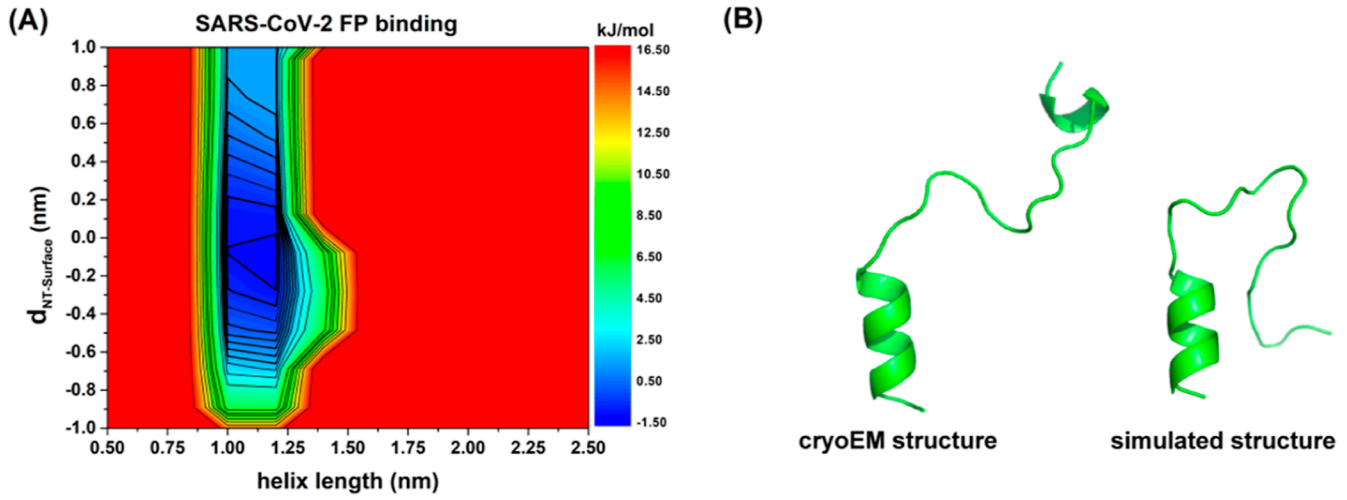

Figure 10. (A) 2D free energy map (kJ/mol) for binding the SARS-CoV-2 FP to the POPC/POPE/cholesterol bilayer membrane. The *x* axis represents the helix length of the FP, while the *y* axis represents the distance ($d_{NT-Surface}$) from the N-terminus of the FP to the bilayer membrane surface. (B) CryoEM structure of SARS-CoV-2 FP (left) taken from an experiment (PDB: 6XR8), and the simulated structure of SARS-CoV-2 FP (right) taken from a representative snapshot for the most stable membrane-bound configuration of the FP with the bilayer membrane.

membrane and the N-terminal helix of the SARS-CoV-1 FP remains unfolded. In the C-terminal binding mode (state I), it is seen that the non-polar side chains of two C-terminal residues (F815 and L823) are pointed toward the bilayer membrane center (Figure S6B of Supporting Information), indicating that the penetrating residues (F815 and L823) have strong interactions with the membrane, consistent with the result shown in Figure 5C.

However, as for the SARS-CoV-2 FP-membrane binding, only the N-terminal binding mode is the most favorable because the short N-terminal helix of FP is deeply embedded in the bilayer membrane, as shown in Figure 8. This observation should support the MD simulation work of Hummer and co-workers,[32] showing that a short amphipathic helix might endow the FP with a high membrane-anchoring strength. In addition, it is interesting to find that the non-polar side chains of three N-terminal residues (F817, I818, and L821) are also buried inside the membrane (Figure S7 of Supporting Information). Furthermore, by comparing the interaction strength of the three N-terminal residues (Phe, Ile, and Leu) with membrane cholesterol (given in Figure 5C,D), it is seen that the three penetrating residues of SARS-CoV-2 FP interact with membrane cholesterol more strongly than those of SARS-CoV-1 FP, suggesting that the hydrophobic residues (Phe, Ile, and Leu) in a short α-helix bind to the cell membrane more strongly than in a long α-helix.

The comparison of FP structures shows that the helix length of the SAR-CoV-1 FP is longer than that of the SAR-CoV-2 FP, as shown in Figure 1. However, we found that the N-terminal helix of the SARS-CoV-1 FP partially unfolded during the transition from the N-terminal binding mode to the C-terminal binding mode. Thus, it is interesting to investigate the correlation between the FP membrane-binding modes and the helix length of the FPs. In this study, we constructed the 2D free energy map as a function of the helix length of the FPs (Figure 9A), showing that the helix length of the SARS-CoV-1 FP was maintained in the N-terminal insertion mode (state a or state V in Figure 7C). However, we found that in the C-

https://doi.org/10.1021/acs.jpcb.2c01295
J. Phys. Chem. B 2022, 126, 4261−4271

terminal loop insertion mode (state c or state I in Figure 7C), the FP helix at the N-terminus was exposed to the aqueous solution and partially unfolded and the helix length of the FP was almost shortened by half (from 1.9 to 1.0 nm). Based on the DSSP[50] analysis results (Figure S8 of Supporting Information), we discovered that the SARS-CoV-1 FP retained the helicity at the N-terminus in two out of the six MD simulations, while there was an observable loss in the α-helical character of the FP in four out of the six MD trajectories. In addition, the DSSP analysis revealed that the C-terminal residues preferred the loop structure (coil-turn-coil or coil-bend-coil) while the N-terminal α-helix was partially unfolded. From the end-to-end distance analysis (Figure S9 of Supporting Information), we observed that the FP with a short helix restrained the distribution of end-to-end distance compared with the FP with a long helix, indicating that the tertiary structure (with a short helix at the N-terminus and a loop structure at the C-terminus) should be stable. Meanwhile, the calculated free energies (or PMFs) of the conformations along the pathway (shown in Figure 9A) revealed the rapid transition between the two binding modes with different FP helix lengths, presented in Figure 9B. Therefore, it is clearly seen from Figures 7B and 9B that the SARS-CoV-1 FP has two favorable binding modes: the C-terminal loop insertion mode with a short α-helix and the N-terminal binding mode with a long α-helix.

In contrast, the helix length of the SARS-CoV-2 FP can be stably maintained in the membrane-bound configurations, as shown in Figure 10. This observation is reasonable because the short N-terminal helix of the SARS-CoV-2 FP can be completely embedded in the bilayer membrane (as shown in Figure 8B). The DSSP analysis and the end-to-end distance analysis gave consistent results (Figures S10 and S11 of Supporting Information), showing that the SARS-CoV-2 FP continuously retained the helicity at the N-terminus. In addition, the DSSP analysis results demonstrated that the C-terminal residues (at least 10 amino acid residues) were unstructured (mainly random coil), and the random coil at the C-terminus would not be conducive to the binding of C-terminal residues to the membrane. Thus, the SARS-CoV-2 FP prefers the N-terminal binding mode because a short helix at the N-terminus endows the SARS-CoV-2 FP with higher membrane-anchoring strength.

CONCLUSIONS

In this work, based on the cryoEM structures of the SARS-CoV-1 and SARS-CoV-2 S-proteins, we constructed different membrane-binding models of the SARS-CoV-1 and SARS-CoV-2 FPs with a lipid composition (POPC/POPE/cholesterol: 60/10/30 mol %). For each FP (SARS-CoV-1 FP or SARS-CoV-2 FP), we simulated six different membrane-binding systems independently using the CHARMM36 force field, and a total of 3.0 μs MD simulation trajectory was used to analyze the membrane-binding mode of the FPs. The all-atom MD simulation results revealed that the binding strength of the SARS-CoV-2 FP to the bilayer membrane is greater than that of the SARS-CoV-1 FP. Meanwhile, we found that the SARS-CoV-2 FP binds to the bilayer membrane favorably with the N-terminal helix insertion mode because the short α-helix at the N-terminus is stable and the C-terminal residues are unstructured. In contrast, the SARS-CoV-1 FP has no such preference, and both the C-terminal loop insertion mode and the N-terminal insertion mode are favorable. Furthermore, we found that the membrane-penetrating residues (Phe, Ile, and Leu) were more likely to interact with membrane cholesterol, suggesting that these hydrophobic residues are essential to the FP−membrane binding. In particular, the membrane-penetrating residues of short α-helix interact with the cell membrane more strongly than those of long α-helix, explaining that the SARS-CoV-2 FP prefers the N-terminal binding to the membrane compared to the SARS-CoV-1 FP.

ASSOCIATED CONTENT

Supporting Information

The Supporting Information is available free of charge at https://pubs.acs.org/doi/10.1021/acs.jpcb.2c01295.

Number density profiles for the choline and phosphate groups of phospholipids, PMF profiles for binding the SARS-CoV-1 and SARS-CoV-2 FPs to the bilayer surface, starting configurations used for constant-velocity pulling simulations, snapshots obtained from pulling a representative configuration of the SARS-CoV-1 FP model and the SARS-CoV-2 FP model, favorable membrane-binding modes of SARS-CoV-1 and SARS-CoV-2 FPs, DSSP analysis of SARS-CoV-1 and SARS-CoV-2 FPs, and the 2D free energy map for end-to-end distance analysis of SARS-CoV-1 and SARS-CoV-2 FPs (PDF)

AUTHOR INFORMATION

Corresponding Author

Hujun Shen − *Guizhou Provincial Key Laboratory of Computational Nano-Material Science, Guizhou Education University, Guiyang 550018, China;* orcid.org/0000-0001-6117-0597; Email: hujun.shen@hotmail.com

Authors

Zhenhua Wu − *Department of Computer Science, Guizhou Vocational Technology College of Electronics & Information, Kaili 556000, China*

Ling Chen − *Guizhou Provincial Key Laboratory of Computational Nano-Material Science, Guizhou Education University, Guiyang 550018, China*

Complete contact information is available at: https://pubs.acs.org/10.1021/acs.jpcb.2c01295

Notes

The authors declare no competing financial interest.

ACKNOWLEDGMENTS

This research was supported by the National Natural Science Foundation of China (no. 22167007), the National Natural Science Foundation of China (no. 21863002), the Science and Technology Foundation of Guizhou Province (no. QKHJC-[2020]1Y040), the start-up fund from Guizhou Education University, and the construction project for Guizhou Provincial Key Disciplines (no. ZDXK[2015]10). The China supercomputing technology (CST) cloud and Shanghai Supercomputer Center (SSC) are gratefully acknowledged for providing the computational resources for the simulations.

REFERENCES

(1) Du, L.; He, Y.; Zhou, Y.; Liu, S.; Zheng, B.-J.; Jiang, S. The spike protein of SARS-CoV - a target for vaccine and therapeutic development. *Nat. Rev. Microbiol.* **2009**, *7*, 226−236.

(2) Wu, F.; Zhao, S.; Yu, B.; Chen, Y.-M.; Wang, W.; Song, Z.-G.; Hu, Y.; Tao, Z.-W.; Tian, J.-H.; Pei, Y.-Y.; et al. A New Coronavirus Associated with Human Respiratory Disease in China. *Nature* **2020**, *579*, 265−269.
(3) Zhou, P.; Yang, X.-L.; Wang, X.-G.; Hu, B.; Zhang, L.; Zhang, W.; Si, H.-R.; Zhu, Y.; Li, B.; Huang, C.-L.; et al. A Pneumonia Outbreak Associated with a New Coronavirus of Probable Bat Origin. *Nature* **2020**, *579*, 270−273.
(4) Holmes, K. V. SARS-Associated Coronavirus. *N. Engl. J. Med.* **2003**, *348*, 1948−1951.
(5) Hofmann, H.; Hattermann, K.; Marzi, A.; Gramberg, T.; Geier, M.; Krumbiegel, M.; Kuate, S.; Überla, K.; Niedrig, M.; Pöhlmann, S. S Protein of Severe Acute Respiratory Syndrome-Associated Coronavirus Mediates Entry into Hepatoma Cell Lines and Is Targeted by Neutralizing Antibodies in Infected Patients. *J. Virol.* **2004**, *78*, 6134−6142.
(6) Whittaker, G. R.; Daniel, S.; Millet, J. K. Coronavirus Entry: How We Arrived at SARS-CoV-2. *Curr. Opin. Virol.* **2021**, *47*, 113−120.
(7) Dodero-Rojas, E.; Onuchic, J. N.; Whitford, P. C. Sterically Confined Rearrangements of SARS-CoV-2 Spike Protein Control Cell Invasion. *eLife* **2021**, *10*, No. e70362.
(8) Walls, A. C.; Park, Y.-J.; Tortorici, M. A.; Wall, A.; McGuire, A. T.; Veesler, D. Structure, Function, and Antigenicity of the SARS-CoV-2 Spike Glycoprotein. *Cell* **2020**, *181*, 281−292.
(9) Kuba, K.; Imai, Y.; Rao, S.; Gao, H.; Guo, F.; Guan, B.; Huan, Y.; Yang, P.; Zhang, Y.; Deng, W.; et al. A Crucial Role of Angiotensin Converting Enzyme 2 (ACE2) in SARS Coronavirus-Induced Lung Injury. *Nat. Med.* **2005**, *11*, 875−879.
(10) Wrapp, D.; Wang, N.; Corbett, K. S.; Goldsmith, J. A.; Hsieh, C.-L.; Abiona, O.; Graham, B. S.; McLellan, J. S. Cryo-EM Structure of the 2019-nCoV Spike in the Prefusion Conformation. *Science* **2020**, *367*, 1260−1263.
(11) Yan, R.; Zhang, Y.; Li, Y.; Xia, L.; Guo, Y.; Zhou, Q. Structural Basis for the Recognition of SARS-CoV-2 by Full-Length Human ACE2. *Science* **2020**, *367*, 1444−1448.
(12) Li, F.; Li, W.; Farzan, M.; Harrison, S. C. Structure of SARS Coronavirus Spike Receptor-Binding Domain Complexed with Receptor. *Science* **2005**, *309*, 1864−1868.
(13) Hoffmann, M.; Kleine-Weber, H.; Schroeder, S.; Krüger, N.; Herrler, T.; Erichsen, S.; Schiergens, T. S.; Herrler, G.; Wu, N.-H.; Nitsche, A.; et al. SARS-CoV-2 Cell Entry Depends on ACE2 and TMPRSS2 and is Blocked by a Clinically Proven Protease Inhibitor. *Cell* **2020**, *181*, 271−280.
(14) Letko, M.; Marzi, A.; Munster, V. Functional Assessment of Cell Entry and Receptor Usage for SARS-CoV-2 and Other Lineage B Betacoronaviruses. *Nat. Microbiol.* **2020**, *5*, 562−569.
(15) Lan, J.; Ge, J.; Yu, J.; Shan, S.; Zhou, H.; Fan, S.; Zhang, Q.; Shi, X.; Wang, Q.; Zhang, L.; et al. Structure of the SARS-CoV-2 Spike Receptor-Binding Domain Bound to the ACE2 Receptor. *Nature* **2020**, *581*, 215−220.
(16) Wang, Q.; Zhang, Y.; Wu, L.; Niu, S.; Song, C.; Zhang, Z.; Lu, G.; Qiao, C.; Hu, Y.; Yuen, K.-Y.; et al. Structural and Functional Basis of SARS-CoV-2 Entry by Using Human ACE2. *Cell* **2020**, *181*, 894−904.
(17) Walls, A. C.; Tortorici, M. A.; Snijder, J.; Xiong, X.; Bosch, B.-J.; Rey, F. A.; Veesler, D. Tectonic Conformational Changes of a Coronavirus Spike Glycoprotein Promote Membrane Fusion. *Proc. Natl. Acad. Sci. U.S.A.* **2017**, *114*, 11157−11162.
(18) Roy, S.; Jaiswar, A.; Sarkar, R. Dynamic Asymmetry Exposes 2019-nCoV Prefusion Spike. *J. Phys. Chem. Lett.* **2020**, *11*, 7021−7027.
(19) Belouzard, S.; Chu, V. C.; Whittaker, G. R. Activation of the SARS Coronavirus Spike Protein via Sequential Proteolytic Cleavage at Two Distinct Sites. *Proc. Natl. Acad. Sci. U.S.A.* **2009**, *106*, 5871−5876.
(20) Bosch, B. J.; Martina, B. E. E.; Van Der Zee, R.; Lepault, J.; Haijema, B. J.; Versluis, C.; Heck, A. J. R.; De Groot, R.; Osterhaus, A. D. M. E.; Rottier, P. J. M. Severe Acute Respiratory Syndrome Coronavirus (SARS-CoV) Infection Inhibition Using Spike Protein Heptad Repeat-Derived Peptides. *Proc. Natl. Acad. Sci. U.S.A.* **2004**, *101*, 8455−8460.
(21) Sainz, B.; Rausch, J. M.; Gallaher, W. R.; Garry, R. F.; Wimley, W. C. Identification and Characterization of the Putative Fusion Peptide of the Severe Acute Respiratory Syndrome-Associated Coronavirus Spike Protein. *J. Virol.* **2005**, *79*, 7195−7206.
(22) Guillén, J.; Pérez-Berná, A. J.; Moreno, M. R.; Villalaín, J. A Second SARS-CoV S2 Glycoprotein Internal Membrane-Active Peptide. Biophysical Characterization and Membrane Interaction. *Biochemistry* **2008**, *47*, 8214−8224.
(23) Madu, I. G.; Roth, S. L.; Belouzard, S.; Whittaker, G. R. Characterization of a highly Conserved Domain within the Severe Acute Respiratory Syndrome Coronavirus Spike Protein S2 Domain with Characteristics of a Viral Fusion Peptide. *J. Virol.* **2009**, *83*, 7411−7421.
(24) Pattnaik, G. P.; Meher, G.; Chakraborty, H. Exploring the Mechanism of Viral Peptide-Induced Membrane Fusion. *Adv. Exp. Med. Biol.* **2018**, *1112*, 69−78.
(25) Chakraborty, H.; Bhattacharjya, S. Mechanistic Insights of Host Cell Fusion of SARS-CoV-1 and SARS-CoV-2 from Atomic Resolution Structure and Membrane Dynamics. *Biophys. Chem.* **2020**, *265*, 106438.
(26) Birtles, D.; Lee, J. Identifying Distinct Structural Features of the SARS-CoV-2 Spike Protein Fusion Domain Essential for Membrane Interaction. *Biochemistry* **2021**, *60*, 2978−2986.
(27) Lai, A. L.; Millet, J. K.; Daniel, S.; Freed, J. H.; Whittaker, G. R. The SARS-CoV Fusion Peptide Forms an Extended Bipartite Fusion Platform that Perturbs Membrane Order in a Calcium-Dependent Manner. *J. Mol. Biol.* **2017**, *429*, 3875−3892.
(28) Guillén, J.; de Almeida, R. F. M.; Prieto, M.; Villalaín, J. Structural and Dynamic Characterization of the Interaction of the Putative Fusion Peptide of the S2 SARS-CoV Virus Protein with Lipid Membranes. *J. Phys. Chem. B* **2008**, *112*, 6997−7007.
(29) Padhi, A. K.; Rath, S. L.; Tripathi, T. Accelerating COVID-19 Research Using Molecular Dynamics Simulation. *J. Phys. Chem. B* **2021**, *125*, 9078−9091.
(30) Remington, J. M.; McKay, K. T.; Ferrell, J. B.; Schneebeli, S. T.; Li, J. Enhanced Sampling Protocol to Elucidate Fusion Peptide Opening of SARS-CoV-2 Spike Protein. *Biophys. J.* **2021**, *120*, 2848−2858.
(31) Borkotoky, S.; Dey, D.; Banerjee, M. Computational Insight Into the Mechanism of SARS-CoV-2 Membrane Fusion. *J. Chem. Inf. Model.* **2021**, *61*, 423−431.
(32) Schaefer, S. L.; Jung, H.; Hummer, G. Binding of SARS-CoV-2 Fusion Peptide to Host Endosome and Plasma Membrane. *J. Phys. Chem. B* **2021**, *125*, 7732−7741.
(33) Gorgun, D.; Lihan, M.; Kapoor, K.; Tajkhorshid, E. Binding Mode of SARS-CoV-2 Fusion Peptide to Human Cellular Membrane. *Biophys. J.* **2021**, *120*, 2914−2926.
(34) Gui, M.; Song, W.; Zhou, H.; Xu, J.; Chen, S.; Xiang, Y.; Wang, X. Cryo-electron Microscopy Structures of the SARS-CoV Spike Glycoprotein Reveal a Prerequisite Conformational State for Receptor Binding. *Cell Res.* **2017**, *27*, 119−129.
(35) Cai, Y.; Zhang, J.; Xiao, T.; Peng, H.; Sterling, S. M.; Walsh, R. M., Jr.; Rawson, S.; Rits-Volloch, S.; Chen, B. Distinct Conformational States of SARS-CoV-2 Spike Protein. *Science* **2020**, *369*, 1586−1592.
(36) Yan, R.; Zhang, Y.; Li, Y.; Ye, F.; Guo, Y.; Xia, L.; Zhong, X.; Chi, X.; Zhou, Q. Structural basis for the different states of the spike protein of SARS-CoV-2 in complex with ACE2. *Cell Res.* **2021**, *31*, 717−719.
(37) Klauda, J. B.; Venable, R. M.; Freites, J. A.; O'Connor, J. W.; Tobias, D. J.; Mondragon-Ramirez, C.; Vorobyov, I.; Mackerell, A. D., Jr.; Pastor, R. W. Update of the CHARMM All-Atom Additive Force Field for Lipids: Validation on Six Lipid Types. *J. Phys. Chem. B* **2010**, *114*, 7830−7843.

https://doi.org/10.1021/acs.jpcb.2c01295
J. Phys. Chem. B 2022, 126, 4261−4271

(38) Jo, S.; Kim, T.; Iyer, V. G.; Im, W. CHARMM-GUI: A web-based graphical user interface for CHARMM. *J. Comput. Chem.* **2008**, *29*, 1859−1865.
(39) Meher, G.; Bhattacharjya, S.; Chakraborty, H. Membrane Cholesterol Modulates Oligomeric Status and Peptide-Membrane Interaction of Severe Acute Respiratory Syndrome Coronavirus Fusion Peptide. *J. Phys. Chem. B* **2019**, *123*, 10654−10662.
(40) MacKerell, A. D.; Bashford, D.; Bellott, M.; Dunbrack, R. L.; Evanseck, J. D.; Field, M. J.; Fischer, S.; Gao, J.; Guo, H.; Ha, S.; et al. All-atom Empirical Potential for Molecular Modeling and Dynamics Studies of Proteins. *J. Phys. Chem. B* **1998**, *102*, 3586−3616.
(41) Jorgensen, W. L.; Chandrasekhar, J.; Madura, J. D.; Impey, R. W.; Klein, M. L. Comparison of Simple Potential Functions for Simulating Liquid Water. *J. Chem. Phys.* **1983**, *79*, 926−935.
(42) MacKerell, A. D.; Feig, M.; Brooks, C. L. Extending the treatment of backbone energetics in protein force fields: limitations of gas-phase quantum mechanics in reproducing protein conformational distributions in molecular dynamics simulations. *J. Comput. Chem.* **2004**, *25*, 1400−1415.
(43) Hess, B.; Kutzner, C.; van der Spoel, D.; Lindahl, E. GROMACS 4: Algorithms for Highly Efficient, Load-Balanced, and Scalable Molecular Simulation. *J. Chem. Theory Comput.* **2008**, *4*, 435−447.
(44) Parrinello, M.; Rahman, A. Polymorphic Transitions in Single Crystals: A New Molecular Dynamics Method. *J. Appl. Phys.* **1981**, *52*, 7182−7190.
(45) Nosé, S. A Unified Formulation of the Constant Temperature Molecular Dynamics Methods. *J. Chem. Phys.* **1984**, *81*, 511.
(46) Hoover, W. G. Canonical Dynamics: Equilibrium Phase-Space Distributions. *Phys. Rev. A* **1985**, *31*, 1695.
(47) Hess, B. P-LINCS: A Parallel Linear Constraint Solver for Molecular Simulation. *J. Chem. Theory Comput.* **2008**, *4*, 116−122.
(48) Darden, T.; York, D.; Pedersen, L. Particle mesh Ewald: AnN·log(N) method for Ewald sums in large systems. *J. Chem. Phys.* **1993**, *98*, 10089−10092.
(49) Song, W.; Corey, R. A.; Ansell, T. B.; Cassidy, C. K.; Horrell, M. R.; Duncan, A. L.; Stansfeld, P. J.; Sansom, M. S. P. PyLipID: A Python Package for Analysis of Protein-Lipid Interactions from Molecular Dynamics Simulations. *J. Chem. Theory Comput.* **2022**, *18*, 1188−1201.
(50) Kabsch, W.; Sander, C. Dictionary of Protein Secondary Structure: Pattern Recognition of Hydrogen-Bonded and Geometrical Features. *Biopolymers* **1983**, *22*, 2577−2637.

https://doi.org/10.1021/acs.jpcb.2c01295
J. Phys. Chem. B 2022, 126, 4261−4271